

ROAD BOUNDARY DETECTION AND TRACKING FOR STRUCTURED AND UNSTRUCTURED ROADS USING A 2D LIDAR SENSOR

J. HAN¹⁾, D. KIM²⁾, M. LEE²⁾ and M. SUNWOO^{3)*}

¹⁾Electronics Development Team 2, Advanced Electronics, Electronics R&D Center, Mando Global R&D Division, Mando Global R&D Center, 21 Pangyo-ro, 255 Beon-gil, Bundang-gu, Seongnam-si, Gyeonggi 463-400, Korea

²⁾Department of Automotive Engineering, Graduate School, Hanyang University, Seoul 133-791, Korea

³⁾Department of Automotive Engineering, Hanyang University, Seoul 133-791, Korea

(Received 30 April 2012; Revised 16 December 2012; Accepted 17 July 2013)

ABSTRACT—Road boundaries can give useful information for evaluating safe vehicle paths in intelligent vehicles. Much previous research has studied road boundary detection, using different types of sensors such as vision, radar, and lidar. Lidar sensors, in particular, show advantages for road boundary extraction including high resolution and wide field of view. However, none of the previous studies examined the problem of detecting road boundaries when roads could be either structured or unstructured. In this study, we developed a road boundary detection and tracking algorithm using lidar sensing for both structured and unstructured roads. The algorithm extracts road features as line segments in polar coordinates relative to the lidar sensor. The extracted road features are then tracked with respect to a vehicle's local coordinates using a nearest neighbor filter. The proposed algorithm accurately detected the road boundaries regardless of the road type.

KEY WORDS : Lidar, Nearest neighbor filter, Road boundary

1. INTRODUCTION

To improve road safety and driving comfort, intelligent vehicle technologies including driver assistance, collision avoidance, and collision notification are rapidly growing worldwide. In intelligent vehicle technologies, perception of obstacles and roads around the vehicle is very important for safe driving in order to generate and evaluate safe vehicle paths.

Roads can be classified into two types: structured and unstructured. The term structured generally refers to roads, such as highways and city roads, with clear markings such as lanes and curbs. Structured roads, therefore, are typically detected by extracting these road markings. Roads which are unstructured have no artificial markings, for example, rural roads. Compared to structured roads, unstructured roads are more difficult to detect owing to unclear road boundaries, low contrast, and arbitrary road shape.

A number of studies have been done to detect the roads using different types of sensing technologies, such as vision, radar, and lidar. Vision-based methodologies detecting lane marks on the structured roads have been extensively evaluated: the rapid adapting lateral position handler (RALPH) (Pomerleau, 1995), generic obstacle and lane detection (GOLD) (Bertozzi and Broggi, 1998), and random sample consensus (RANSAC) and Kalman filter

based lane tracking and forward vehicle detection (Choi *et al.*, 2012) are examples of these. Other vision-based methods have been used to study unstructured roads: the supervised classification applied to road following (SCARF) (Crisman and Thorpe, 1993), the unsupervised clustering applied to road following (UNSCARF) (Crisman and Thorpe, 1991), and the vision-based road transportation for unmanned operation on urban-like scenarios (VIRTUOUS) (Sotelo *et al.*, 2004). Although all these vision-based methods have advantages including high information content, low operating power, low cost, and a passive noninvasive sensor, these methods are less effective under complex illumination, shadows, or bad weather.

Radar sensors can provide road images up to 200 m ahead in haze, dust, rain, and snow. Several approaches have been studied to detect the roads using radar-based methods (Lakshmanan and Grimmer, 1996; Ma *et al.*, 2000; Tsang *et al.*, 2006). However, these methods are not appropriate for low vehicle speeds and non-luxury vehicles owing to low resolution, narrow horizontal field of view (FOV), and high cost of radar sensors.

Lidar sensors have higher resolution, wider FOV, and lower cost than radar sensors. Performance of lidar sensors in adverse weather has also shown improvement (Arita *et al.*, 2007; Boehlau *et al.*, 2009). Lidar-based methods for road detection are classified according to the types of extracted features. One class consists of obstacle detection methods, in which the lidar sensor is looking forward at

*Corresponding author. e-mail: msunwoo@hanyang.ac.kr

features such as vehicles, posts, and guardrails (Kirchner and Heinrich, 1998; Takagi *et al.*, 2006; Weiss *et al.*, 2007). Other methods extract roads, or road marks such as lanes and curbs, while the lidar sensor is looking down the road ahead (Cramer and Wanielik, 2002; Fardi *et al.*, 2003; Wijesoma *et al.*, 2004; Cremean and Murray, 2006; Takagi *et al.*, 2006; Fardi *et al.*, 2007; Kodagoda *et al.*, 2007; Peterson *et al.*, 2008; Lindner *et al.*, 2009).

Lidar-based road detection methods using obstacle extraction can be suitable for well-structured highways with guardrails and posts (Kirchner and Heinrich, 1998; Weiss *et al.*, 2007). However, lower obstacles such as curbs in urban roads cannot be detected. Lane marks extraction methods using lidar sensors are not appropriate for roads in which the lane marks cannot be detected in the same manner as with vision-based methods (Takagi *et al.*, 2006; Lindner *et al.*, 2009). Road extraction using minimum roughness is not suited to conditions including variable road widths and complex roughness, as may be found in urban roads (Cremean and Murray, 2006). Curb extraction methods work with line segments corresponding to the vertical surfaces of curbs using a downward looking front-mounted 2D lidar sensor (Wijesoma *et al.*, 2004; Kodagoda *et al.*, 2007). However, these methods are suited only to urban roads with curbs. Additionally, these curb detection and tracking methods depend on localization of the vehicle with respect to global coordinates, which is a nontrivial problem that has been the subject of extensive research (Toledo-Moreo *et al.*, 2007; Skog and Handel, 2009; Jo *et al.*, 2010; Jo *et al.*, 2012). The curb extraction by the longest straight line is not suitable for narrow roads or obstacle existing roads (Kim *et al.*, 2007; Kang *et al.*, 2012).

In this study, a road boundary detection and tracking method using a lidar sensor with respect to a vehicle's local coordinates is presented. This method can be applied to both structured and unstructured roads by extracting line segments as road features in polar coordinates with a 2D lidar sensor. In particular, the road line segments are extracted and selected by using the pitch and roll angle of the 2D lidar sensor corresponding to the possible vehicle

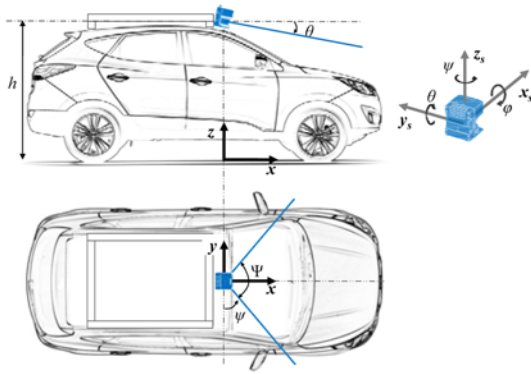


Figure 1. Configuration of a 2D lidar sensor, vehicle coordinates, and sensor coordinates.

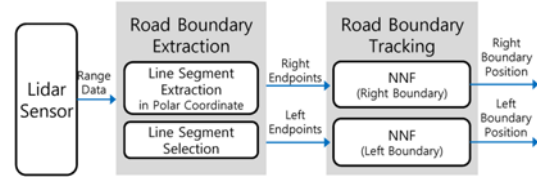


Figure 2. System architecture.

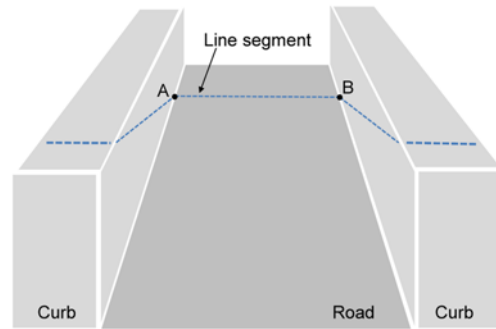
motion. This method can be applied to any roads regardless of the road type such as no-curb and narrow roads.

The extracted road features are tracked using the nearest neighbor filter (NNF) algorithm, which is the most widely used algorithm for target tracking in clutter owing to its computational simplicity (Li and BarShalom, 1996).

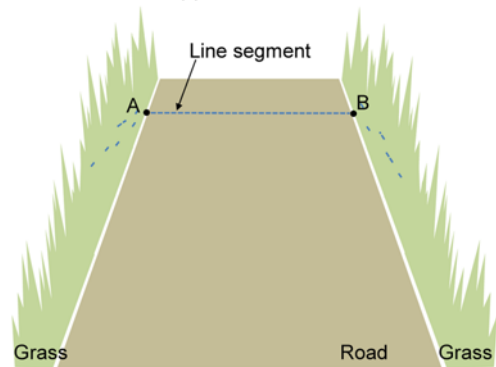
The rest of this paper is organized as follows. In section 2, a system overview of the road boundary detection and tracking is described. In section 3, feature extraction of the road boundaries in polar coordinates from range data of the 2D lidar sensor is presented. In section 4, road boundary tracking using the NNF is explained. In section 5, experimental results are presented for structured and unstructured road conditions. Conclusions are discussed in section 6.

2. SYSTEM OVERVIEW

In order to perceive road boundaries, a 2D lidar sensor is



(a) Structured road

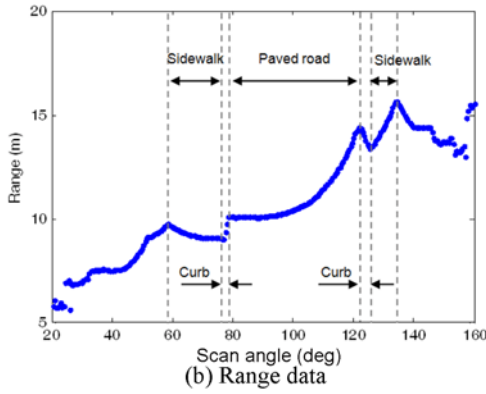


(b) Unstructured road

Figure 3. Ideal line segments in structured and unstructured roads.



(a) Road scene

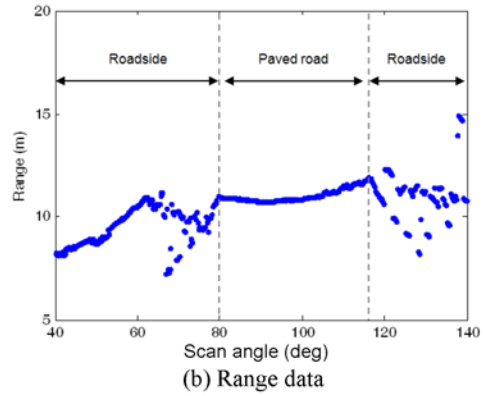


(b) Range data

Figure 4. Raw data from a 2D lidar sensor for a structured road with curbs.



(a) Road scene



(b) Range data

Figure 5. Raw data from a 2D lidar sensor for a structured road without curbs.

installed so as to look down the road ahead, as shown in Figure 1. The lidar sensor scans the road surface from height h , with pitch angle θ , scan angle ψ , and scan angle range Ψ . Figure 2 shows a system architecture for road boundary perception. The system consists of three parts. First, the lidar sensor generates range data in polar coordinates. Next, line segments are extracted from the range data, taking into account the height and pitch of the lidar sensor. Figure 3 shows ideal line segments in structured and unstructured roads. In structured roads, the line segments may be contained in the road, curbs, and sidewalks; on the other hand, in unstructured roads, the line segments lie primarily in the road because of the presence of grass, bushes, and roadside trees. Among all the extracted line segments, those which may represent road surfaces are selected.

Each selected line segment has a left and a right endpoint. In Figure 3, for example, the points A and B are the left and right endpoints of the line segment on the road. The left and right endpoints become measurement outputs for tracking the left and right road boundary, respectively. Finally, the positions of the left and right road boundary are determined using two NNFs.

3. ROAD BOUNDARY EXTRACTION

3.1. Line Segment Extraction

The 2D lidar sensor gives range data in polar coordinates. Figure 4 ~ Figure 6 show examples of the raw data from the 2D lidar sensor for structured and unstructured roads. The range data corresponding to the paved road in Figure 4 (b) and Figure 5 (b) is smoother than the range data from the unpaved road in Figure 6 (b). Moreover, Figure 4 (b) shows low noise levels for range data associated with the roadside region because of curbs, sidewalks, and buildings. The range data in polar coordinates of the lidar sensor can be converted to local vehicle coordinates x , y , and z by sequence of consecutive rotations about z_s , x_s , and y_s axes, as shown in Figure 1, using the height, pitch, and roll of the 2D lidar sensor:

$$\begin{bmatrix} x_i \\ y_i \\ z_i \end{bmatrix} = \begin{bmatrix} 0 \\ 0 \\ h \end{bmatrix} + \mathbf{R}_{y_s}(\theta) \mathbf{R}_{x_s}(\varphi) \mathbf{R}_{z_s}(\psi_i) \begin{bmatrix} 0 \\ -\rho_i \\ 0 \end{bmatrix} \quad (1)$$

$$= \begin{bmatrix} \rho_i (\sin \psi_i \cos \theta - \cos \psi_i \sin \theta \sin \varphi) \\ -\rho_i \cos \psi_i \cos \varphi \\ h - \rho_i (\sin \psi_i \sin \theta + \cos \psi_i \cos \theta \sin \varphi) \end{bmatrix}$$

where ψ_i is the i th scan angle as yaw angle, ρ_i is the i th range measurement, h is the height, θ is the pitch angle, and φ is the roll angle. The range data (ρ_i, ψ_i) in polar coordinates was represented as $[0 \ -\rho_i \ 0]^T$ with a rotation of ψ_i about the z_s -axis in Cartesian coordinates.

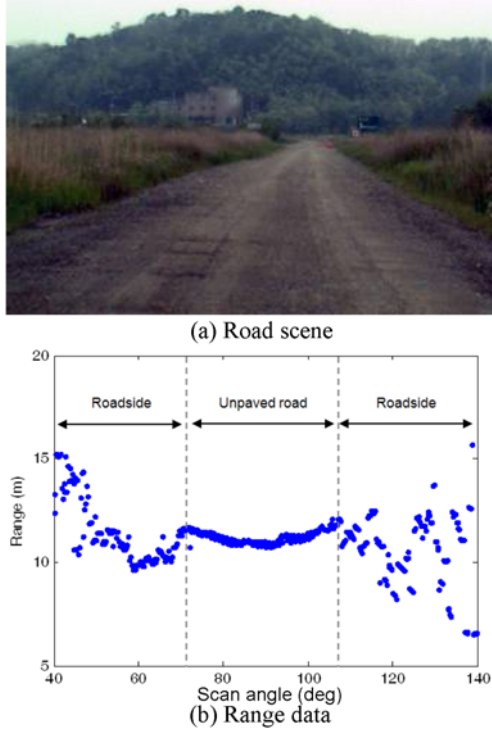


Figure 6. Raw data from a 2D lidar sensor for an unstructured road.

$\mathbf{R}_y(\theta)$, $\mathbf{R}_x(\varphi)$, and $\mathbf{R}_z(\psi_i)$ are rotation matrices for counter clockwise rotation of pitch, roll, and yaw angles about the each axis defined as (Jazar, 2008):

$$\mathbf{R}_y(\theta) = \begin{bmatrix} \cos \theta & 0 & \sin \theta \\ 0 & 1 & 0 \\ -\sin \theta & 0 & \cos \theta \end{bmatrix} \quad (2)$$

$$\mathbf{R}_x(\varphi) = \begin{bmatrix} 1 & 0 & 0 \\ 0 & \cos \varphi & -\sin \varphi \\ 0 & \sin \varphi & \cos \varphi \end{bmatrix} \quad (3)$$

$$\mathbf{R}_z(\psi_i) = \begin{bmatrix} \cos \psi_i & -\sin \psi_i & 0 \\ \sin \psi_i & \cos \psi_i & 0 \\ 0 & 0 & 1 \end{bmatrix} \quad (4)$$

In order to extract line segments, any of several line extraction methods can be applied to the transformed data in Cartesian coordinates (Borges and Aldon, 2004; Nguyen *et al.*, 2007). Coordinate conversion for an entire dataset can, however, be computationally expensive.

Thus, in this study, we proposed a line extraction method in polar coordinates considering height, roll angle and pitch angle of the sensor without the coordinate conversion. This line extraction approach was based on the *Iterative-End-Point-Fit* (IEPF) algorithm (Borges and Aldon, 2004; Duda and Hart, 1973). First, breakpoints associated with discontinuous measurements are obtained; this breakpoint detection allows the algorithm to distinguish sequences of

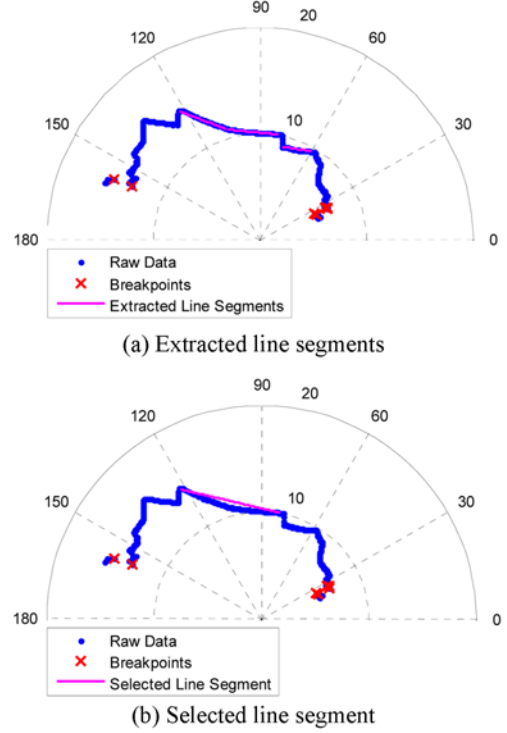


Figure 7. Line segment extraction for a structured road with curbs in a polar plot.

measurements which are not interrupted by changes in surfaces during scanning. Then the line segments are acquired in each continuous scan sequence from the range data.

3.1.1. Breakpoint detection

An adaptive breakpoint detection algorithm was used to find discontinuities in the range data. If the difference between consecutive range data ρ_i and ρ_{i-1} is larger than an adaptive threshold value, D_{max} , which was then the i th and $(i-1)$ st scan points are regarded as the breakpoints, as described in the following algorithm (Borges and Aldon, 2004):

```

01  FOR  $i = 2$  to  $N_s$ 
02     $D_{max} = \rho_{i-1} ( \sin(\lambda) / \sin(\lambda - \Delta\psi) - 1 ) + \varepsilon$ 
03    IF  $|\rho_i - \rho_{i-1}| > D_{max}$  THEN
04      The  $i$  and  $i-1$  th points are the breakpoints
05    ENDIF
06  ENDFOR
```

where N_s is the number of range data points, $\Delta\psi$ is the angular resolution of the sensor, ε is an offset representing sensor noise, and λ is a threshold angle used as a design parameter to extrapolate the worst acceptable range point ρ_i . Figure 7~9 show examples of the breakpoint detection in polar coordinates applied to structured and unstructured roads. In Figure 7, the range data has few breakpoints since the structures, such as curbs, sidewalks, and buildings,

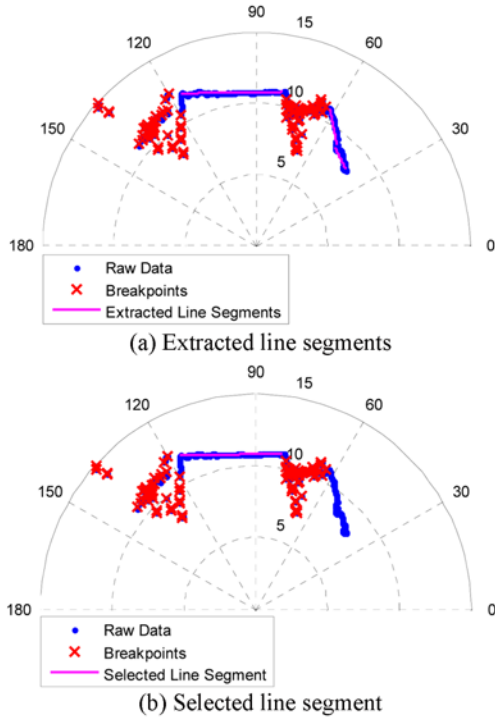


Figure 8. Line segment extraction for a structured road without curbs in a polar plot.

have continuous surfaces. On the other hand, many breakpoints exist in Figure 8 and 9 because of plants such as grass, bushes, and road side trees, which have irregular shapes.

3.1.2. Line segment extraction

In order to extract the line segments in polar coordinates, we observe first that the range measurement for a flat road is a function of the height, pitch, and roll of the 2D lidar sensor from (1), as follows (Cremean and Murray, 2006):

$$\rho_i = \frac{h}{\sin \psi_i \sin \theta + \cos \psi_i \cos \theta \sin \psi} \quad (5)$$

Thus, for a certain height, pitch, and roll of the sensor, the line segment contains a set of the range data satisfying (5). Using (5), a regression model can be represented for two range data in the continuous scan sequence as

$$\begin{bmatrix} \tan \psi_{n_s} \\ \tan \psi_{n_e} \end{bmatrix} \begin{bmatrix} \alpha \\ \beta \end{bmatrix} = \begin{bmatrix} h / (\rho_{n_s} \cos \psi_{n_s}) \\ h / (\rho_{n_e} \cos \psi_{n_e}) \end{bmatrix} \quad (6)$$

where $\alpha = \sin \theta$, $\beta = \cos \theta \sin \varphi$, and n_s and n_e are the respective indices of the first and last range data points for a region of the continuous scan. Then the pitch and roll of the sensor for the line segment connecting between n_s and n_e scan points can be determined by the least-squares method as follows:

$$\begin{bmatrix} \alpha \\ \beta \end{bmatrix} = \left(\begin{bmatrix} \tan \psi_{n_s} & 1 \\ \tan \psi_{n_e} & 1 \end{bmatrix} \begin{bmatrix} \tan \psi_{n_s} & 1 \\ \tan \psi_{n_e} & 1 \end{bmatrix}^T \right)^{-1} \begin{bmatrix} \tan \psi_{n_s} & 1 \\ \tan \psi_{n_e} & 1 \end{bmatrix}^T \begin{bmatrix} h / (\rho_{n_s} \cos \psi_{n_s}) \\ h / (\rho_{n_e} \cos \psi_{n_e}) \end{bmatrix} \quad (7)$$

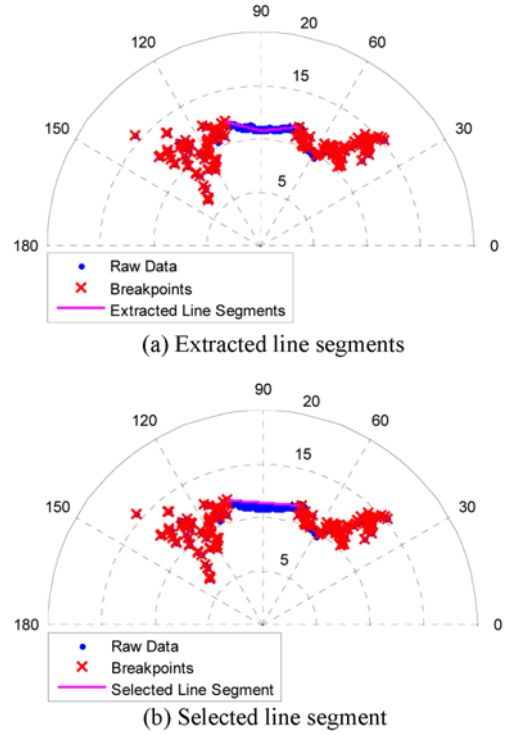


Figure 9. Line segment extraction for a structured road without curbs in a polar plot.

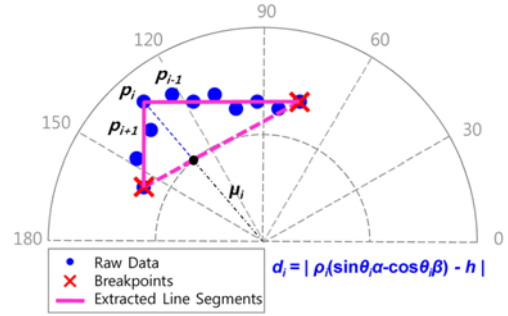


Figure 10. IEPF algorithm in polar coordinates.

Accordingly, the other scan points between n_s and n_e can be evaluated for inclusion in the same line segment using the IEPF algorithm as shown in Figure 10. IEPF algorithm in polar coordinates.. In this figure, μ_i is the i th estimated range data point from the sensor to the dashed line segment, given by

$$\mu_i = \frac{h}{\sin \psi_i \alpha + \cos \psi_i \beta} \quad (8)$$

Then the i th height difference d_i of the measured range data relative to the dashed line segment can be obtained by the formula

$$\begin{aligned} d_i &= |(\rho_i - \mu_i)(\sin \psi_i \alpha + \cos \psi_i \beta)| \\ &= |\rho_i(\sin \psi_i \alpha + \cos \psi_i \beta) - h| \end{aligned} \quad (9)$$

If the maximum height difference d_{max} is larger than a threshold height difference d_{Th} , then the line segment is split into two line segments. Otherwise, the scan points n_s and n_e become the endpoints of the line segment, and points between n_s and n_e points are included in the same line segment as follows:

```

01  $n_e = 1$ 
02 WHILE  $n_e \leq N_s$ 
03    $n_s = n_e$  /* Index of the first point of the region */
04    $n_e = n_s + 1$  /* Index of the last point of the region */
05   WHILE  $n_e$  point is not a breakpoint
06      $n_e = n_e + 1$  /* Search the last point of the region */
07   IF  $n_e = N_s$  THEN
08     BREAK
09   ENDIF
10 ENDWHILE
11 WHILE  $n_e - n_s + 1 > N_{min}$  /* Check the min. number */
12   Obtain  $\alpha$  and  $\beta$  by (7) /* Calculate the pitch and roll */
13   FOR  $i = n_s$  to  $n_e$ 
14     Compute  $d_i$  by (9) /* Compute the difference */
15   ENDFOR
16    $d_{max} = \max(d_i)$  /* Obtain the maximum difference */
17   IF  $d_{max} > d_{Th}$  THEN /* Split the line segment */
18      $n_e =$  the index of  $d_{max}$  scan point
19   ELSEIF /* Extract the line segment */
20      $n_s$  and  $n_e$  points are endpoints of a line segment
21     BREAK
22   ENDIF
23 ENDWHILE
24 ENDWHILE

```

* N_{min} Minimum number of scan points constituting a line segment

Examples of the line segment extraction in polar coordinates are shown in Figure 7~9 (a).

3.2. Line Segment Selection

The extracted line segments may include not only road surfaces but also roadside objects such as curbs, sidewalks, and buildings. In order to reduce the number of the extracted line segments not corresponding to the road surface, the following line selection criteria were applied.

- (1) *Minimum number of scan points constituting a line segment*: all line segments must have elements more than a minimum number of scan points, N_{min} ; this condition is already used for the line segment extraction because of the reduction in computation time.
- (2) *Minimum road width*: all line segments must be longer than a minimum road width, L_{min} . This criterion selects line segments corresponding to roads which a vehicle can pass through.
- (3) *Maximum variations of sensor pitch and roll angles*: for all line segments, the variation of the pitch and roll parameters must be smaller than the maximum values Θ_{max} and Φ_{max} respectively. For an ideal flat road, the line segment representing the road exhibits no sensor pitch or roll. This criterion can select the road line segment among the extracted line segments although other vehicles and obstacles exist on the road.

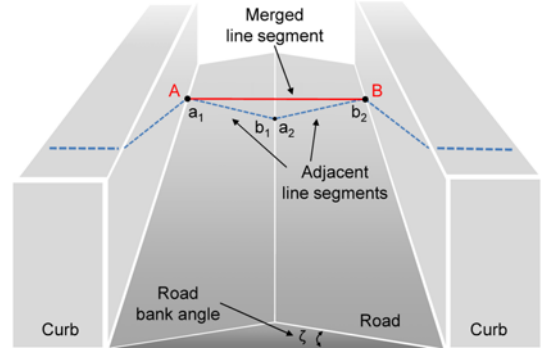


Figure 11. Combination of extracted line segments considering a road bank angle.

- (4) *Combination of two adjacent line segments considering road bank angle*: two adjacent line segments can be merged into one line segment as shown in Figure 11. The differences in the indices and the range measurements of the two adjacent endpoints, e.g., b_1 and a_2 in Figure 11, must be smaller than I_{max} and P_{max} respectively. In addition, the difference in roll parameter values of the two adjacent line segments must be smaller than Z_{max} .

Figure 7~9 (b) show examples of a selected line segment in the range of polar coordinates. In Figure 7, it can be seen that two adjacent line segments are merged into one line segment in a structured road because of the road bank angle. A similar result is shown for an unstructured road in Figure 9.

The selected line segment has two endpoints, left and right. The range data for each endpoint in polar coordinates

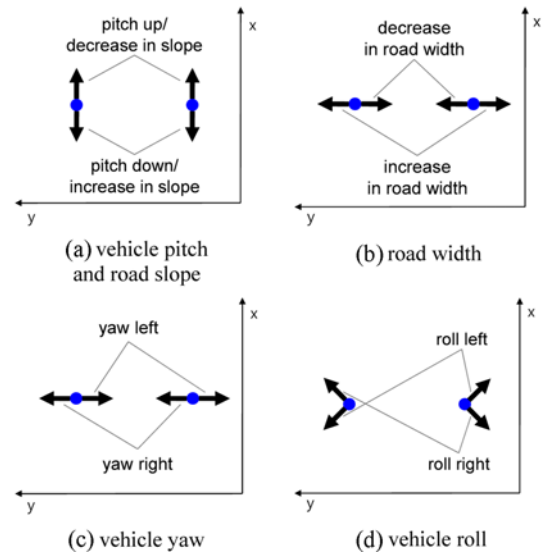


Figure 12. Motion of road boundary targets depending on vehicle motion and road geometry.

can be converted to vehicle x and y coordinates using (1). The transformed left and right endpoints become measurement outputs for tracking the left and right road boundaries, respectively.

4. ROAD BOUNDARY TRACKING

4.1. Target Model

Road boundary targets with respect to local vehicle coordinates change depending on vehicle motion and road geometry, as shown in Figure 12. In this figure (a), the targets move forward and backward in the local coordinates when the pitch up and down respectively. In this figure (c) and (d), the yaw and roll motions cause the targets to move left, right, up, and down in the local coordinates. Changes in road geometry, e.g., road slope and road width, also induce the target motion in local coordinates in this figure (a) and (b). In particular, because road geometry varies according to the road environment, the motion of road boundary targets in local coordinates cannot be easily defined. Thus, in this study, a free motion model was used to represent the road boundary targets that can be appropriate to any vehicle motion and road geometry, as follows:

$$\begin{aligned} \mathbf{s}_{k+1} &= \mathbf{A}\mathbf{s}_k + \mathbf{w}_k \\ &= \begin{bmatrix} 1 & 0 & T_s & 0 \\ 0 & 1 & 0 & T_s \\ 0 & 0 & 1 & 0 \\ 0 & 0 & 0 & 1 \end{bmatrix} \mathbf{s}_k + \mathbf{w}_k \end{aligned} \quad (10)$$

$$\begin{aligned} \mathbf{z}_k &= \mathbf{C}\mathbf{s}_k + \mathbf{v}_k \\ &= \begin{bmatrix} 1 & 0 & 0 & 0 \\ 0 & 1 & 0 & 0 \end{bmatrix} \mathbf{s}_k + \mathbf{v}_k \end{aligned} \quad (11)$$

where $\mathbf{s} = [x, y, \dot{x}, \dot{y}]$; T_s is the sampling period; and \mathbf{w} and \mathbf{v} are independent, zero-mean, Gaussian noise variables for process and measurement respectively, with respective covariances \mathbf{R}_w and \mathbf{R}_v .

4.2. Nearest Neighbor Filter (NNF)

The NNF is one of the most widely used methods for target tracking in clutter owing to its computational simplicity (Li and BarShalom, 1996). The NNF assumes that the NN measurement is target-originated, and applies a standard Kalman filter to update the state estimate of the target using the NN measurement. Although the NN measurement may be originated from a clutter, the low computational load is a big advantage in a real-time target tracking in clutter. Moreover, in this study, the NNF was suitable for the road boundary tracking because the line segment extraction and selection algorithm can reduce the number of false measurements.

The operation of the NNF is shown in Figure 13. First, the initial state and error covariance values are determined.

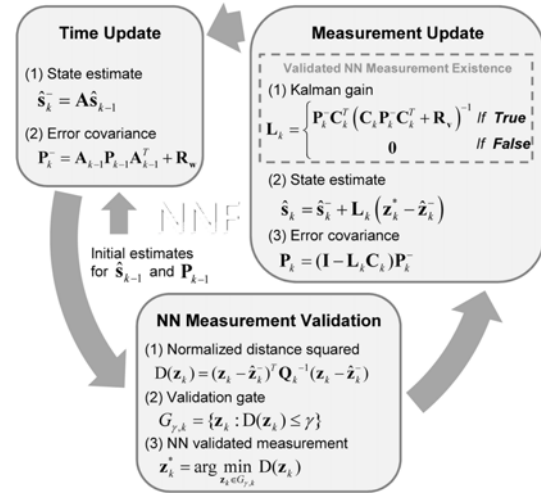


Figure 13. Operation of a nearest neighbor filter.

Then, the *priori* state $\hat{\mathbf{s}}_k^-$ and error covariance \mathbf{P}_k^- are predicted using the target model as follows

$$\hat{\mathbf{s}}_k^- = \mathbf{A}\hat{\mathbf{s}}_{k-1} \quad (12)$$

$$\mathbf{P}_k^- = \mathbf{A}\mathbf{P}_{k-1}\mathbf{A}^T + \mathbf{R}_w \quad (13)$$

Next, measurements are evaluated using an ellipsoidal validation gate. Only measurements falling inside the validation gate are deemed to be generated from the target of interest. Otherwise, the measurement is regarded as invalid. The ellipsoidal validation gate at time k is defined as

$$G_{\gamma,k} = \{\mathbf{z}_k : D(\mathbf{z}_k) \leq \gamma\} \quad (14)$$

in which $g = \sqrt{\gamma}$ is the gate size and the normalized distance squared (NDS) $D(\mathbf{z}_k)$ is defined by

$$D(\mathbf{z}_k) = (\mathbf{z}_k - \hat{\mathbf{z}}_k^-)^T \mathbf{Q}_k^{-1} (\mathbf{z}_k - \hat{\mathbf{z}}_k^-) \quad (15)$$

Here $\hat{\mathbf{z}}_k^- = \mathbf{C}\hat{\mathbf{s}}_k^-$ is the predicted measurement from the *priori* state, and $\mathbf{Q}_k = \mathbf{C}_k \mathbf{P}_k^- \mathbf{C}_k^T + \mathbf{R}_v$ is the measurement residual covariance. Among the validated measurements, the NN measurement at time k , \mathbf{z}_k^* , is determined by

$$\mathbf{z}_k^* = \arg \min_{\mathbf{z}_k \in G_{\gamma,k}} D(\mathbf{z}_k) \quad (16)$$

In the measurement update, if an NN validated measurement exists, then the *posteriori* state \mathbf{s}_k and error covariance \mathbf{P}_k are corrected using the formulae

$$\mathbf{s}_k = \hat{\mathbf{s}}_k^- + \mathbf{L}_k (\mathbf{z}_k^* - \hat{\mathbf{z}}_k^-) \quad (17)$$

$$\mathbf{P}_k = (\mathbf{I} - \mathbf{L}_k \mathbf{C}_k) \mathbf{P}_k^- \quad (18)$$

where the Kalman gain, \mathbf{L}_k , is defined as

$$\mathbf{L}_k = \mathbf{P}_k^+ \mathbf{C}_k^T (\mathbf{C}_k \mathbf{P}_k^+ \mathbf{C}_k^T + \mathbf{R}_v)^{-1} \quad (19)$$

If there is no validated measurement, then

$$\hat{\mathbf{s}}_k = \hat{\mathbf{s}}_k^- \quad (20)$$

$$\mathbf{P}_k = \mathbf{P}_k^- \quad (21)$$

5. EXPERIMENTAL RESULTS

5.1. Experimental Setup

In order to evaluate the road boundary detection and tracking algorithm, a test vehicle was equipped with a downward looking 2D lidar sensor (SICK LMS291-S05, Sick, 2012), a differential GPS (DGPS), and an inertial measurement unit (IMU), as shown in Figure 1 and 14. The DGPS and IMU were used for the localization of the test vehicle as in (Jo *et al.*, 2010; Gwak *et al.*, 2013). To facilitate comparison with road scenes, the results of the road boundary detection and tracking in local coordinates were transformed to global coordinates. Table 1 shows configuration parameter values for the lidar sensor, which was installed looking downward 10 m ahead of the vehicle. A scan angle range of 100 degrees was used, with a scan angular resolution of 0.25 degrees. Design parameters for road boundary extraction and tracking are presented in Tables 2 and 3. In the experiments, three types of roads were considered: a structured road with curbs, a structured road without curbs, and an unstructured road.

5.2. Structured Road with Curbs

For structured roads with curbs, two types of test roads



Figure 14. Test vehicle.

Table 1. Configuration parameters for a Lidar sensor.

Parameter	Definition	Value
h	height	1.75 m
φ	pitch	9.9 deg
ψ	roll	0 deg
ω	scan angle range	100 deg
$\Delta\theta$	scan angular resolution	0.25 deg

Table 2. Design parameters for road boundary extraction.

Parameter	Definition	Value
Breakpoint detection		
λ	threshold angle	10 deg
ε	offset	0.09 m
Line segment extraction		
N_{min}	minimum number of scan points constituting a line segment	24
d_{Th}	threshold height difference	0.06 m
Line Segment Selection		
L_{min}	minimum road width	3 m
Θ_{max}	maximum variation in lidar sensor pitch angle	5 deg
Φ_{max}	maximum variation in lidar sensor roll angle	7 deg
I_{max}	maximum difference in indices of two adjacent endpoints	3
P_{max}	maximum difference in range values of two adjacent endpoints	0.1 m
Z_{max}	maximum difference in roll angles of two adjacent endpoints	7 deg

Table 3. design parameters for road boundary tracking.

Parameter	Definition	Value
Target model		
T_s	sampling period	50 ms
Nearest neighbor filter		
g	gate size	1
\mathbf{R}_w	covariance of process noise	$\begin{bmatrix} 1 & 0 & 0 & 0 \\ 0 & 1 & 0 & 0 \\ 0 & 0 & 0.01 & 0 \\ 0 & 0 & 0 & 0.01 \end{bmatrix}$
\mathbf{R}_v	covariance of measurement noise	$\begin{bmatrix} 0.01 & 0 \\ 0 & 0.01 \end{bmatrix}$
$\hat{\mathbf{S}}_0$	initial estimate of state for right and left	$\begin{bmatrix} 3 & 10 & 0 & 0 \\ -3 & 10 & 0 & 0 \end{bmatrix}^T$
\mathbf{P}_0	initial estimate of error covariance	$\begin{bmatrix} 1 & 0 & 0 & 0 \\ 0 & 1 & 0 & 0 \\ 0 & 0 & 0 & 0 \\ 0 & 0 & 0 & 0 \end{bmatrix}$

were considered, as shown in Figure 15. The first test road was the road in a campus, illustrated in Figure 4 (a), which exhibits a significant change in elevation as shown in Figure 16. The second test road was a normal city road.

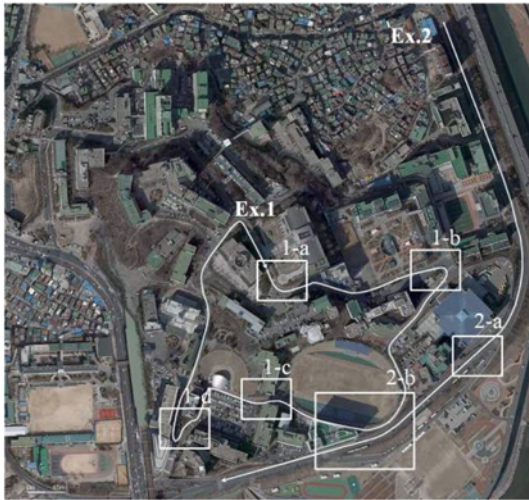


Figure 15. Test roads 1 and 2 for structured roads with curbs.

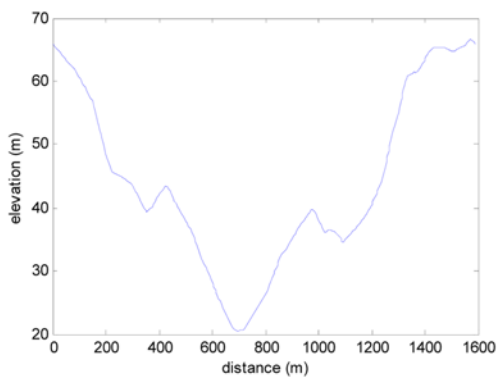


Figure 16. Elevation of a structured road with curbs 1.

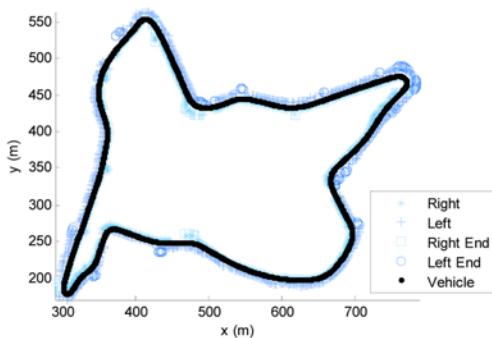


Figure 17. Experimental results for a structured road with curbs 1.

Figure 17 shows experimental results for the first test road. The vehicle speed was 10–40 km/h during the test. Detailed road scenes and experimental results for four regions in the first test road are displayed in Figure 18. In Figure 17 and 18, the right and left curbs are detected as

Table 4. Experimental Results of Road Boundary Detection.

Experiment	Road boundary	Detection rate	False positive
Structured road with curbs 1	Left	81.4%	2.4%
	Right	85.7%	2.7%
Structured road with curbs 2	Left	92.5%	1.1%
	Right	85.8%	1.1%
Structured road without curbs	Left	95.7%	2.6%
	Right	97.9%	4.5%
Unstructured road	Left	92.0%	0.8%
	Right	96.0%	0.2%

road boundaries. In these results, the road boundaries are not presented when NN measurements are not validated by the gate. The lateral detection range was limited to about 12 m owing to 100 degree scan angle range. Therefore, the right and left boundaries due to the limited lateral detection range are presented as the right and left ends respectively. These right and left ends can detect crossroads as shown in Figure 18 (a), (b), and (c). These results can be also applied to sensor data fusions with map data at intersections (Shooter and Reeve, 2009; Roessler and Fuerstenberg, 2009). Figure 19 shows the experimental results for the second test road. The vehicle speed was 50–80 km/h during this test. The detailed road scenes and experimental results for two regions are presented in Figure 20. As with the first test road, the road boundaries were detected and right and left ends are presented, as shown in Figure 19 and 20. The experimental results show over 80% detection rate with less than 3% false positive rate in the both test roads, as shown in Table 4. The detection rate is calculated by the ratio of the validated NN measurement existence. In the intersection entrance, the right, left, or both road boundaries should be quickly disappeared and represented by the right or left end. The detection rate of the first test road is a little lower than other road types because of more intersection existence. In the second test road, right detection rate is lower than the left because more intersections exist in the right side of the road. The false positives are caused by high variation in the elevation which can make high change of the vehicle pose.

5.3. Structured Road without Curbs

A road scene for a test road in a suburban area is shown in Figure 5 (a). The test road has a width of 6.5 m, with two lanes and no curb. The vehicle speed was 30–50 km/h during the test. Figure 21 and Figure 22 show good experimental results for the test road without curbs. As shown in Figure 22 (a), the road boundaries are well detected when the road is straight. At the corner, the left ends are presented due to the limited scan angle range, as

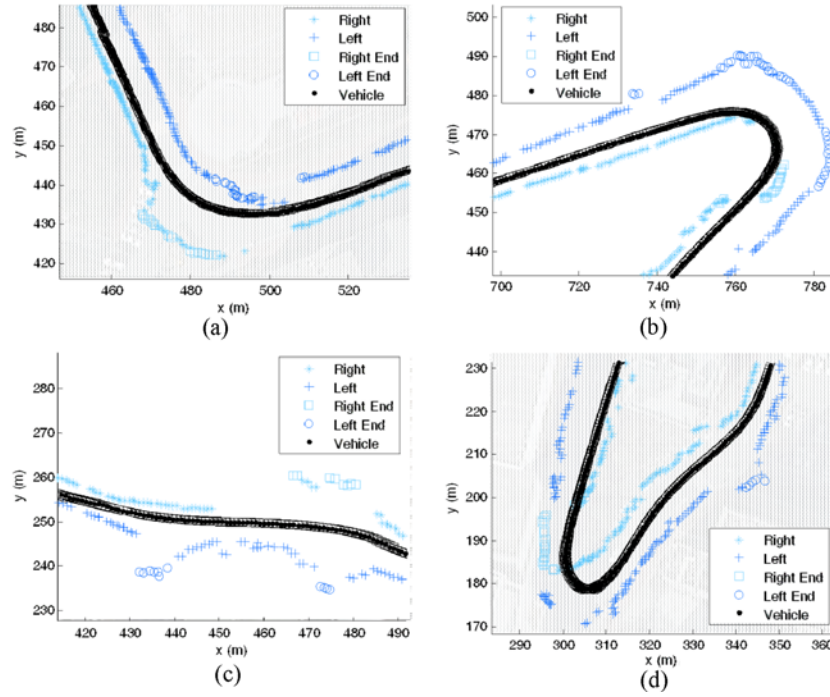


Figure 18. Detailed experimental results and road scenes of four regions of a structured road with curbs 1.

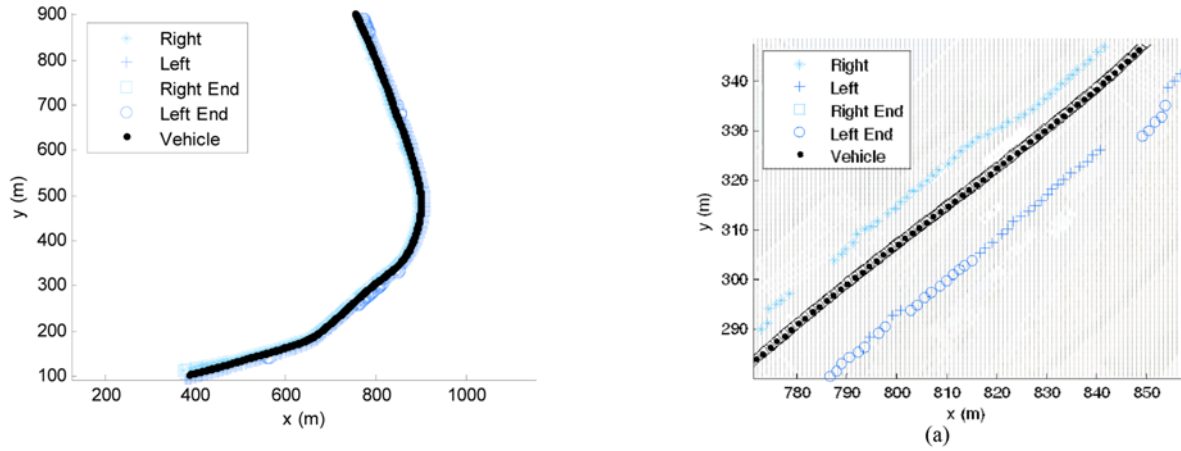


Figure 19. Experimental results for a structured road with curbs 2.

shown in Figure 22 (b). The experimental results show over 95% detection rate with less than 5% false positive rate, as shown in Table 4. In addition, all these false positives have a little lateral distance error because roadside grasses cover the road edge.

5.4. Unstructured Road

Figure 23 shows a road scene and experimental results for a off-road in a rural area. The detailed road scenes and experimental results are presented in Figure 24. The vehicle speed was 30–50 km/h during the test. In Figure 24, good experimental results are shown, despite the large pitch and roll motions of the test vehicle caused by the

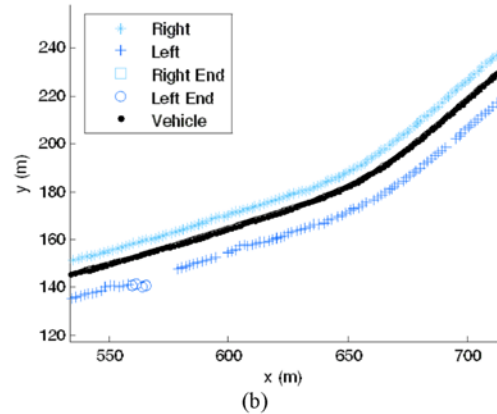


Figure 20. Detailed experimental results and road scenes of two regions of a structured road with curbs 2.

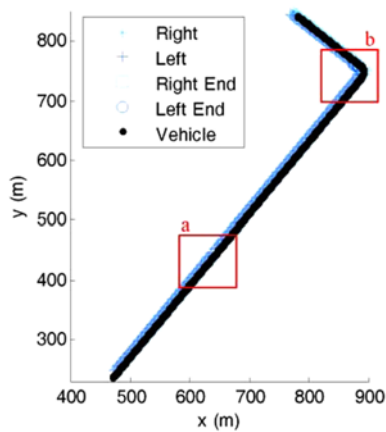


Figure 21. Experimental results for a structured road without curbs.

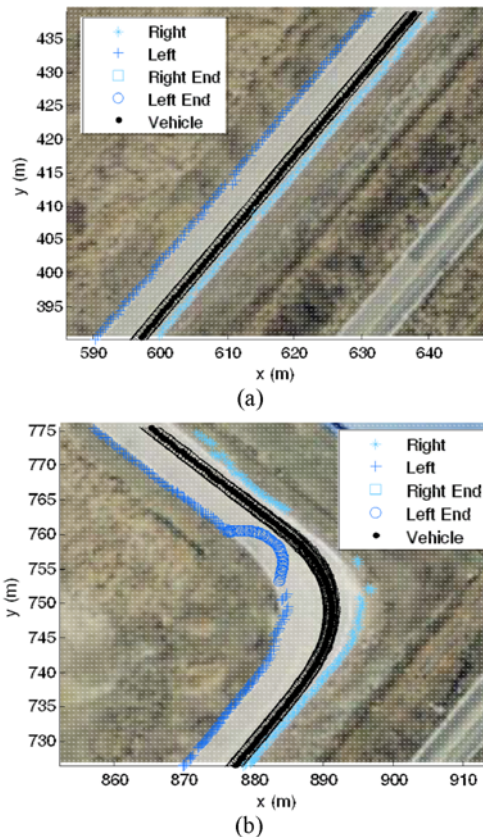


Figure 22. Detailed experimental results of two regions of a structured road without curbs.

uneven ground. The experimental results show over 92% detection rate with less than 0.8% false positive rate, as shown in Table 4.

6. CONCLUSION

In this study, a road boundary detection and tracking

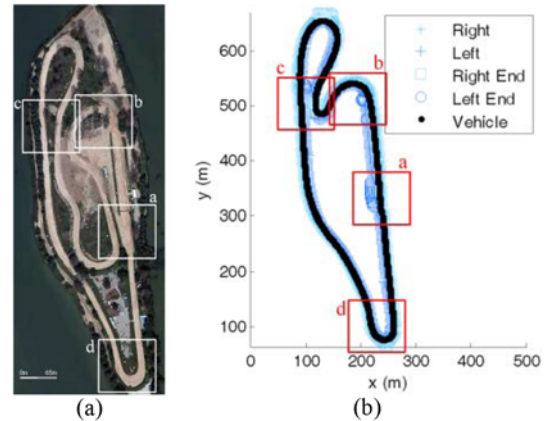


Figure 23. Experimental results for an unstructured road: (a) road scene of a test road, and (b) experimental results.

algorithm for structured and unstructured roads using a lidar sensor was discussed. The algorithm extracts line segments from the roads; the endpoints of these line segments are then tracked using an NNF. In the experimental results for both structured and unstructured roads, the algorithm provided accurate road boundaries regardless of the road type. In adverse weather or conditions including icy and wet roads, the current technology of the sensor cannot obtain accurate range data. For this reason, the road boundary cannot be accurately detected by the lidar sensor. However, the improvement of the performance for the lidar sensor in adverse conditions can enhance the performance of the road boundary detection. In addition, distant road boundaries cannot be detected by using only lidar sensor. This disadvantage can overcome by the multi-sensor fusion methods with a vision-based technology. The results of the road boundary detection and tracking by the lidar sensor, therefore, can be applied to the planning and evaluation of safe vehicle paths as well as for sensor data fusion in intelligent vehicle applications.

ACKNOWLEDGEMENT—This work was supported in part by the National Research Foundation of Korea grant funded by the Korea government (MEST) (No. 2011-0017495), by the Ministry of Knowledge Economy (MKE), by the Korea Institute for Advancement in Technology (KIAT) through the Workforce Development Program in Strategic Technology, by the BK21 plus program under the Ministry of Education of Korea (22A20130000045), and by the Industrial Strategy Technology Development Program of the Ministry of Knowledge Economy under (No.10039673).

REFERENCES

Arita, S., Goff, D., Miyazaki, H. and Ishio, W. (2007). Wide field of view (FOV) and high-resolution lidar for advanced driver assistance systems. *Proc. SAE 2007*

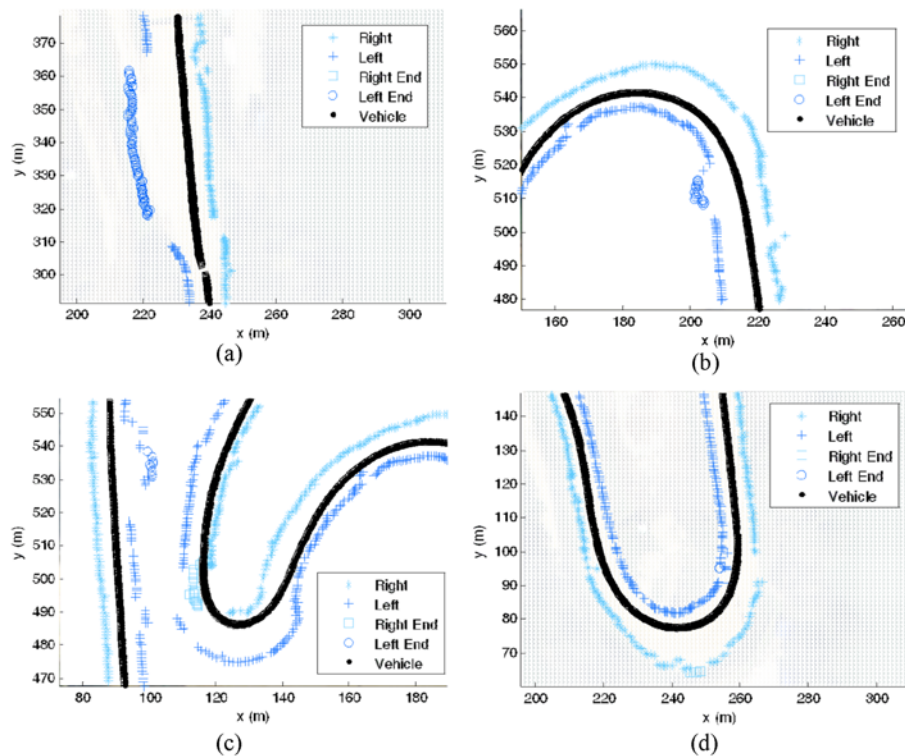


Figure 24. Detailed experimental results and road scenes of four regions of an unstructured road.

World Cong.

- Bertozzi, M. and Broggi, A. (1998). GOLD: A parallel real-time stereo vision system for generic obstacle and lane detection. *IEEE Trans. Image Process.*, **7**, 62–81.
- Boehlau, C., Lichte, B. and Ottenhues, T. (2009). New concept of a compact LIDAR scanner for ACC and safety applications. *Proc. SAE 2009 World Cong., SAE Int'l.*
- Borges, G. A. and Aldon, M. J. (2004). Line extraction in 2D range images for mobile robotics. *J. Intelligent and Robotic Systems*, **40**, 267–297.
- Choi, H.-C., Park, J.-M., Choi, W.-S. and Oh, S.-Y. (2012). Vision-based fusion of robust lane tracking and forward vehicle detection in a real driving environment. *Int. J. Automotive Technology* **13**, **4**, 653–669.
- Cramer, H. and Wanielik, G. (2002). Road border detection and tracking in noncooperative areas with a laser radar system. *German Radar Symp.*
- Cremean, L. and Murray, R. (2006). Model-based estimation of off-highway road geometry using single-axis ladar and inertial sensing. *Proc. IEEE Conf. Robot. and Autom.*, 1661–1666.
- Crisman, J. and Thorpe, C. (1991). UNSCARF: A color vision system for the detection of unstructured roads. *Proc. IEEE Conf. Robot. and Autom.*, 2496–2501.
- Crisman, J. D. and Thorpe, C. E. (1993). SCARF: A color-vision system that tracks roads and intersections. *IEEE Trans. Robot. Autom.*, **9**, 49–58.

- Duda, R. and Hart, P. (1973). *Pattern Recognition and Scene Analysis*. Wiley. New York.
- Fardi, B., Scheunert, U., Cramer, H. and Wanielik, G. (2003). Multi-modal detection and parameter-based tracking of road borders with a laser scanner. *IEEE Intell. Vehicles Symp.*, 95–99.
- Fardi, B., Weigel, H., Wanielik, G. and Takagi, K. (2007). Road border recognition using FIR images and LIDAR signal processing. *Proc. IEEE Intell. Vehicles Symp.*, 1278–1283.
- Gwak, M., Jo, K. and Sunwoo, M. (2013). Neural-network Multiple Models Filter (NMM)-based position estimation system for autonomous vehicles. *Int. J. Automotive Technology* **14**, **2**, 265–274.
- Jazar, R. N. (2008). *Vehicle Dynamics: Theory and Applications*. Springer Verlag.
- Jo, K., Chu, K. and Sunwoo, M. (2012). Interacting multiple model filter-based sensor fusion of GPS with in-vehicle sensors for real-time vehicle positioning. *IEEE Trans. Intelligent Transportation Systems*, **13**, 329–343.
- Jo, K., Chu, K., Lee, K. and Sunwoo, M. (2010). Integration of multiple vehicle models with an IMM filter for vehicle localization. *Proc. IEEE Intell. Vehicles Symp.*
- Kang, Y., Roh, C., Suh, S. and Song, B. (2012). A lidar-based decision-making method for road boundary detection using multiple Kalman filters. *IEEE Trans.*

- Industrial Electronics*, 4360–4368.
- Kim, S., Roh, C., Kang, S. and Park, M. (2007). Outdoor navigation of a mobile robot using differential GPS and curb detection. *Proc. IEEE Conf. Robotics and Automation*.
- Kirchner, A. and Heinrich, T. (1998). Model based detection of road boundaries with a laser scanner. *Proc. IEEE Conf. Intell. Vehicles*, 93–98.
- Kodagoda, K. R. S., Ge, S. S., Wijesoma, W. S. and Balasuriya, A. P. (2007). IMMPDAF approach for road-boundary tracking. *IEEE Trans. Veh. Technol.*, **56**, 478–486.
- Lakshmanan, S. and Grimmer, D. (1996). A deformable template approach to detecting straight edges in radar images. *IEEE Trans. Pattern Anal. Mach. Intell.*, **18**, 438–443.
- Li, X. R. and BarShalom, Y. (1996). Tracking in clutter with nearest neighbor filters: Analysis and performance. *IEEE Trans. Aerosp. Electron. Syst.*, **32**, 995–1010.
- Lindner, P., Richter, E., Wanielik, G., Takagi, K. and Isogai, A. (2009). Multi-channel lidar processing for lane detection and estimation. *Proc. IEEE Conf. Intell. Transp.*
- Ma, B., Lakshmanan, S. and Hero, A. (2000). Simultaneous detection of lane and pavement boundaries using model-based multisensor fusion. *IEEE Trans. Intell. Transp. Syst.*, **1**, 135–147.
- Nguyen, V., Gaechter, S., Martinelli, A., Tomatis, N. and Siegwart, R. (2007). A comparison of line extraction algorithms using 2D range data for indoor mobile robotics. *Autonomous Robots*, **23**, 97–111.
- Peterson, K., Ziglar, J. and Rybski, P. (2008). Fast feature detection and stochastic parameter estimation of road shape using multiple LIDAR. *Proc. IEEE Intell. Robots and Systems*, 612–619.
- Pomerleau, D. (1995). RALPH: Rapidly adapting lateral position handler. *Proc. IEEE Intell. Vehicles Symp.*, 506–511.
- Roessler, B. and Fuerstenberg, K. (2009). Sensor based intersection reconstruction for a cooperative intersection safety system. *IEEE Conf. Intell. Comput. Commun. and Process*, 393–399.
- Shooter, C. and Reeve, J. (2009). INTERSAFE-2 architecture and specification. *IEEE Conf. Intell. Comput. Commun. and Process.*, 379–386.
- Skog, I. and Handel, P. (2009). In-car positioning and navigation technologies-A survey. *IEEE Trans. Intell. Transp. Syst.*, **10**, 4–21.
- Sotelo, M. A., Rodriguez, F. J. and Magdalena, L. (2004). VIRTUOUS: Vision-based road transportation for unmanned operation on urban-like scenarios. *IEEE Trans. Intell. Transp. Syst.*, **5**, 69–83.
- Takagi, K., Morikawa, K., Ogawa, T. and Saburi, M. (2006). Road environment recognition using on-vehicle LIDAR. *Proc. IEEE Intell. Vehicles Symp.*, 120–125.
- Technical Description of LMS 291 Laser Measurement Systems (2012). www.sick.com
- Toledo-Moreo, R., Zamora-Izquierdo, M. A., Ubeda-Minarro, B. and Gomez-Skarmeta, A. F. (2007). High-integrity IMM-EKF-based road vehicle navigation with low-cost GPS/SBAS/INS. *IEEE Trans. Intell. Transp. Syst.*, **8**, 491–511.
- Tsang, S. H., Hall, P. S., Hoare, E. G. and Clarke, N. J. (2006). Advance path measurement for automotive radar applications. *IEEE Trans. Intell. Transp. Syst.*, **7**, 273–281.
- Weiss, T., Schiele, B. and Dietmayer, K. (2007). Robust driving path detection in urban and highway scenarios using a laser scanner and online occupancy grids. *Proc. IEEE Intell. Vehicles Symp.*, 184–189.
- Wijesoma, W., Kodagoda, K. and Balasuriya, A. (2004). Road-boundary detection and tracking using lidar sensing. *IEEE Trans. Robot. Autom.*, **20**, 456–464.